Acta Oceanol. Sin., 2018, Vol. 37, No. 3, P. 94–102
DOI: 10.1007/s13131-018-1202-8
http://www.hyxb.org.cn
E-mail: hyxbe@263.net

A statistical distribution of quad-pol X-band sea clutter time series acquired at a grazing angle

WANG Yunhua[1, 2], LI Qun[1], ZHANG Yanmin[1*]

[1] College of Information Science &Engineering, Ocean University of China, Qingdao 266100, China

[2] Laboratory for Regional Oceanography and Numerical Modeling, Qingdao National Laboratory for Marine Science and Technology, Qingdao 266237, China

Received 29 August 2017; accepted 13 September 2017

Abstract

Although the complex Wishart distribution has been widely used to analyze the statistic properties of quad-pol SAR spatial data, the applicability of this complex distribution to the time series of sea clutter is rarely discussed. The measured data of the quad-pol X-band marine radar demonstrate that the time series of the sea echoes are also satisfied the circular Gaussian distributions if the low intensity signals, which are mainly dominated by a radar noise, in the shadow regions of the large-scale waves are removed. On the basis of this fact, the probability density functions (PDFs) of the intensity as well as the phase, the real and the imaginary parts of the sea echoes obtained by the marine radar have been derived, and the theoretical models are all expressed in closed forms. In order to validate the theoretical results, the PDFs are compared with the experimental data collected by the McMaster IPIX radar. And the comparisons show that the PDF models are in good agreement with the experimental data.

Key words: sea clutter, quad-pol coherent X-band radar, statistical distribution function

Citation: Wang Yunhua, Li Qun, Zhang Yanmin. 2018. A statistical distribution of quad-pol X-band sea clutter time series acquired at a grazing angle. Acta Oceanologica Sinica, 37(3): 94–102, doi: 10.1007/s13131-018-1202-8

1 Introduction

The statistical characterizations of the radar clutter scattered from the sea surface have always attracted many researchers' attention due to the importance for radar signal processing, especially the detection of targets (Kuttikkad and Chellappa, 1994; Vachon et al., 1997; Brusch et al., 2011). The complicated sea state has a significant impact on scattering properties, and the backscattered sea echoes always have spikier noise that would increase the false alarm rate in a target detection algorithm. In recent years, the X-band marine radar which is usually mounted at the top of a ship or on the seacoast has been widely used to detect ocean targets and ocean waves (Lee et al., 1995; Greco et al., 2004; Hwang et al., 2008; Johnson et al., 2009; Cui et al., 2010; Wang et al., 2015). Therefore, in order to improve the target detection algorithm (Posner, 2002), it is necessary to analyze the sea clutter statistically. The earlier researches were mainly focused on the statistic properties of scattering intensity (Farina et al., 1986; Conte et al., 1991). In the most recent two years, the statistical properties of sea cluster time-series have also been investigated (Yang et al., 2017; Zhu et al., 2017). Yang et al. (2017) found that the amplitude of the sea clutter and the phase difference between HH and VH channels could respectively satisfy log-normal and Gaussian distributions well. However, there is a flaw in this work because of the wrong solution of the phase difference. Zhu et al. (2017) presented the statistical properties of the sea clutter obtained by a Ka-band coherent radar. And the assessments of the suitability of the different theoretical distributions, such as K, Weibull, Pareto, and compound inverse Gaussian (CIG) distributions, to the sea clutter amplitude probability density functions (PDFs) were discussed. For the Ka-band coherent radar, the fitted results reveal that these three distributions simultaneously provide good fits to the data in most range cells for the different radar channels. Recently, with the development of the polarimetric SAR technology, the statistical analysis of polarization parameters has also been studied utilizing the polarimetric synthetic aperture radar (SAR) data. In the earlier works (Lee et al., 1994a, b), based on the complex Wishart distribution theory, the PDFs of the intensity and phase difference between different polarimetric channels had been derived and the theoretical results were compared with pol-SAR data. Up to now, however, less effort has been made to research the polarization features of the sea clutter time-series using the Wishart distribution model.

Just as discussed in Goodman (1963), in order to research the statistical properties of the polarimetric radar signals by the complex Wishart distribution model, the circular Gaussian assumption (i.e., the real and imaginary parts of each radar channels are both random Gaussian variables) should be satisfied. Fortunately, the polarimetric data acquired by the McMaster IPIX radar (Farina et al., 1997) show that the sea clutter time series at grazing angles also satisfy the circular Gaussian distributions. On the basis of this fact, in the present work, the PDFs of the intensity and phase difference as well as the real and imaginary parts of the elements in a covariance matrix have been derived. The comparisons with the experimental data show that the shadow of

Foundation item: The National Key Research and Development Program of China under contract No. 2016YFC1401008; the National Natural Science Foundation of China under contract No. 41376179; the National Natural Science Foundation of China-Shandong Joint Fund for Marine Science Research Centers under contract No. U1406404.

*Corresponding author, E-mail: yanminzhang@ouc.edu.cn

large-scale wave will cause significant effect on the statistical properties of the IPIX radar signals. However, if we remove the low intensity signals in the shadow regions, the remainder signals can fit the theoretical distribution well. Furthermore, the influences of the inhomogeneity of the sea clutter on the PDFs are also discussed in detail. The remaining of this paper is organized as follows: the analysis of the polarimetric sea clutter sequences acquired by the McMaster IPIX Radar is carried out in Section 2, the theoretical PDFs are derived in Section 3, and the comparisons with the measurements and the conclusions are shown in Sections 4 and 5, respectively.

2 Data analysis

In this work, the time series of the sea echoes acquired by the McMaster IPIX radar are analyzed. The radar frequency and the pulse repetition frequency (PRF) are 9.39 GHz and 1 kHz, respectively. As an example, the intensity of the 17th data (19931107_ 135603_starea.cdf) is shown in Fig. 1. Along a range direction, there are 14 resolution cells which ranged from 2 574 to 2 769 m. Along the time axis, the sampling frequency of the radar is 1 kHz. The 8th to 11th cells are the range bins including targets and the other range cells are corresponding to the sea clutter. The warmer color (red) stripes denote the high scattering sea areas where were illuminated by a radar beam. On the contrary, the cooler color (blue) stripes denote the scattering from the shadow regions where the intensity of the scattering fields is obviously lower and mainly dominated by the radar noise (Fig. 2a). Therefore, in order to analyze the statistical properties of the scattering echoes from the sea surface, the pseudo signals in the shadow regions should be removed. Without loss of generality, the short-time normalized Doppler spectrum of the sea clutter from the second range cell is shown in Fig. 2b. In Figs 2a and b, the possible shadow regions are labeled by symbols S1 to S14. It is well known that the Doppler spectrum of the sea clutter always has a spectral peak around the mean Doppler frequency. Nevertheless, the powers of the radar signals in the possible shadow regions are spread over a wide frequency region because the phase differences of the radar noises are randomly distributed in a range of [–π, π]. In Fig. 3, the spectra of the signals from the illuminated and shadow regions are shown. From this figure, we can find that the powers of the scattering fields from the illuminated regions are concentrated around the mean Doppler shift. Thus, the sea clutter can be distinguished from the radar noise by the properties of the Doppler spectrum. Here, we defined a parameter R as

$$R=\int_{f_D-\Delta f}^{f_D+\Delta f} P(f)\mathrm{d}f \Big/ \int_{-500}^{500} P(f)\mathrm{d}f, \tag{1}$$

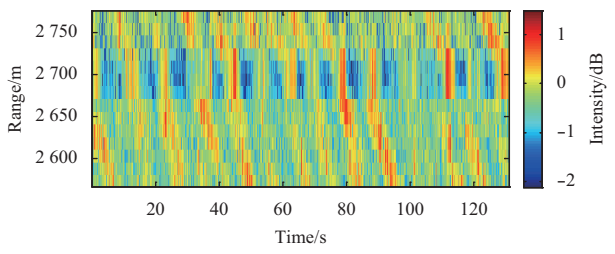

Fig. 1. The range-time distribution of intensity for HH polarization sea clutter.

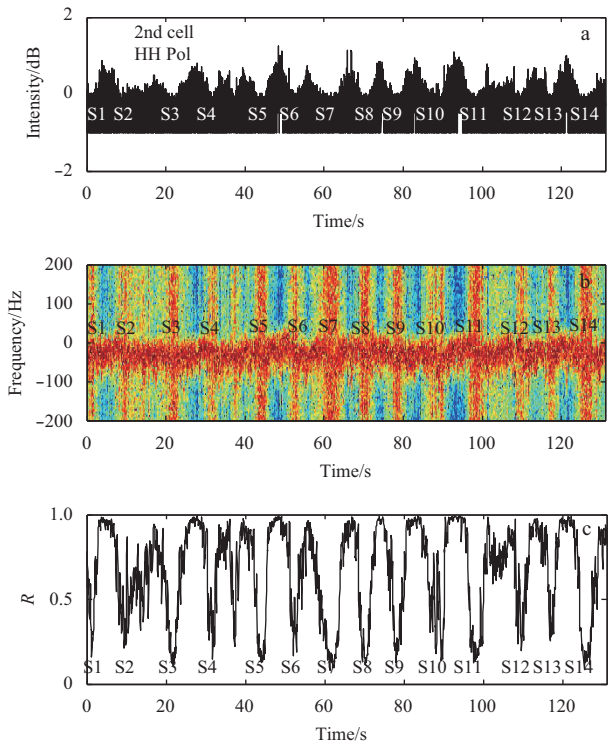

Fig. 2. The intensity (a), the normalized short-time spectrum of the sea clutter time series backscattered from the second range cell (b) and the value of the parameter R (c).

where

$$P(f)=\left|\int_{-T/2}^{T/2} S(t)\exp(-\mathrm{j}2\pi ft)\mathrm{d}t\right|^2, \tag{2}$$

where $P(f)$ is the Doppler spectrum of the radar signals, and $S(t)$ denotes the actual scattering field, and the time length of $S(t)$ is set to 0.2 s, i.e., T = 0.2 s. In Eq. (1), the Doppler shift f_D and the band width Δf can be expressed as

$$f_D=\int_{-500}^{500} P(f)f\mathrm{d}f \Big/ \int_{-500}^{500} P(f)\mathrm{d}f, \tag{3}$$

and

$$\Delta f=\sqrt{\int_{-500}^{500} (f-f_D)^2 P(f)\mathrm{d}f \Big/ \int_{-500}^{500} P(f)\mathrm{d}f}. \tag{4}$$

The parameter R reflects the degree of the concentration of the echo power. And more concentrated the echo power, the greater the value of the parameter R. Just as shown in Fig. 3c, in the illuminated regions, the evaluated mean value of the parameter R is above 0.9. However, the mean value of the parameter R in the shadowed regions labeled by symbols S1 to S14 is only 0.29. Thus, the parameter R can be used as an indicator to distinguish the actual sea clutter from the radar noise. Here, a simple threshold of R is set to be 0.3. Then, we have

$$S_{pq}^{s}=S_{pq} \text{ when } R\geqslant 0.3 \text{ and } S_{pq}^{n}=S_{pq} \text{ when } R<0.3, \tag{5}$$

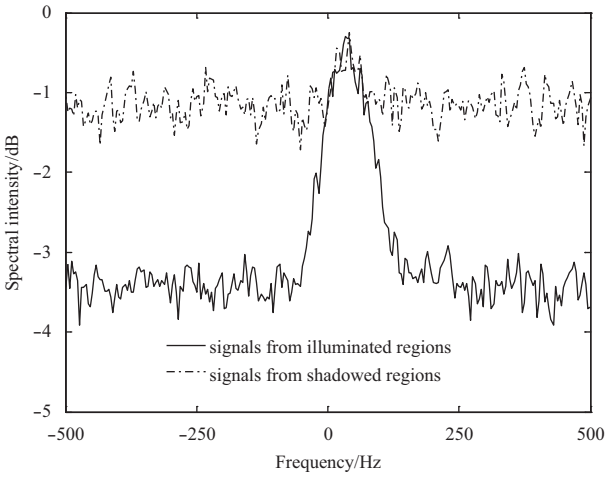

Fig. 3. The mean spectra intensity of the signals from the illuminated and shadowed regions.

where S_{pq} is the raw data acquired by radar. S^{s}_{pq} and S^{n}_{pq} denote the actual sea echo and the noise of radar system, respectively.

In order to study the statistical properties of the polarimetric radar signals by the complex Wishart distribution model, the circular Gaussian assumption (Goodman, 1963), i.e., the following conditions, should be satisfied

$$\langle S^{s}_{pq,\,i}\rangle=\langle S^{s}_{pq,\,r}\rangle=0, \tag{6}$$

$$\langle S^{s}_{pq,\,i}S^{s}_{pq,\,r}\rangle=0, \tag{7}$$

$$\langle S^{s}_{pq,\,i}S^{s}_{uv,\,i}\rangle=\langle S^{s}_{pq,\,r}S^{s}_{uv,\,r}\rangle, \tag{8}$$

$$\langle S^{s}_{pq,\,r}S^{s}_{uv,\,i}\rangle=-\langle S^{s}_{pq,\,i}S^{s}_{uv,\,r}\rangle, \tag{9}$$

where the symbol $\langle\bullet\rangle$ is an averaging operator. $S^{s}_{pq,\,r}$ and $S^{s}_{pq,\,i}$ denote the real and imaginary parts of the actual sea echoes. To verify this assumption, the estimated values from the copolarized actual sea clutter from the second range cell are displayed in Table 1. And the estimated values demonstrate that the actual sea clutters obtained by the IPIX radar satisfy the circular Gaussian assumption well.

To further verify the circular Gaussian assumption, the parameters skewness and kurtosis are also introduced in this work. These two parameters (Conte et al., 2004) are defined as follows:

$$r_3=\frac{\left\langle(x-u)^3\right\rangle}{\left\langle(x-u)^2\right\rangle^{\frac{3}{2}}}, \tag{10}$$

$$r_4=\frac{\left\langle(x-u)^4\right\rangle}{\left\langle(x-u)^2\right\rangle^{2}}-3, \tag{11}$$

where x is the real or imaginary part of the scattering field; and $u=\langle x\rangle$, denotes the mean value. The skewness and the kurtosis are usually adopted to measure the asymmetry and tailedness of a stochastic process. If a stochastic process satisfies the Gaussian distribution, parameters r_3 and r_4 are both equal to 0. As an example, the histograms of the real and imaginary parts of the HH-polarized clutters scattered form the second range cell are shown in Fig. 4. Meanwhile, the values of the skewness and the kurtosis are also estimated. From Figs 4a and b, it is found that the coefficients of the skewness and the kurtosis estimated by the actual sea clutter (S^{s}_{HH}) are both small and the Gaussian distribution model can fit the histograms well. However, just as expected, the skewness and kurtosis evaluated by the raw data (S_{HH}) are relatively larger and the histograms in Figs 4c and d do not satisfy the Gaussian distributions. Here, it should be pointed out that the same conclusions can also be obtained for the data of the other three polarization channels.

From what has been discussed above, it is concluded that the real and imaginary parts of the actual sea clutter satisfy the Gaussian distribution approximately. Thus, for the actual sea clutters, the circular Gaussian assumption is reasonable and the statistical properties could be analyzed by the complex Wishart distribution model.

3 Statistical model

The scattering matrix $\boldsymbol{S}$ of the acquired by the quad-pol radar can be written as

$$\boldsymbol{S}(t)=\begin{bmatrix}S_{HH}(t) & S_{HV}(t)\\ S_{VH}(t) & S_{VV}(t)\end{bmatrix}, \tag{12}$$

where $S_{HH}(t)$, $S_{VH}(t)$, $S_{HV}(t)$ and $S_{VV}(t)$ denote the time-series of different polarization channels. Defining a bivariate vector $\vec{u}$ as

$$\vec{u}(t)=\begin{bmatrix}S_{pq}(t')\\ S_{uv}(t)\end{bmatrix}. \tag{13}$$

Then, the n-look covariance matrix is defined as

$$\boldsymbol{Z}(\tau)=\frac{1}{n}\sum_{k=1}^{n}\vec{u}(t_k)\vec{u}(t'_k)^{*\mathrm{T}}\quad(k=1,2,\cdots,n), \tag{14}$$

where $\tau=t'_k-t_k$, and the superscript *T denotes complex conjugate transpose.

Supposing the real and imaginary parts of the complex ele-

Table 1. The estimated values of the parameters mentioned in Eqs (6)–(9)

Parameters	Estimated values	Parameters	Estimated values
$\langle S^{s}_{HH,\,i}\rangle$	0.014 1	$\langle S^{s}_{HH,\,r}\rangle$	0.026 6
$\langle S^{s}_{HH,\,i}S^{s}_{HH,\,r}\rangle$	0.119 8	$\langle S^{s}_{VV,\,i}S^{s}_{VV,\,r}\rangle$	0.052 3
$\langle S^{s}_{HH,\,r}S^{s}_{VV,\,r}\rangle$	2.363 8	$\langle S^{s}_{HH,\,i}S^{s}_{VV,\,i}\rangle$	2.471 8
$\langle S^{s}_{HH,\,r}S^{s}_{VV,\,i}\rangle$	–0.915 1	$\langle S^{s}_{HH,\,i}S^{s}_{VV,\,r}\rangle$	1.092 4

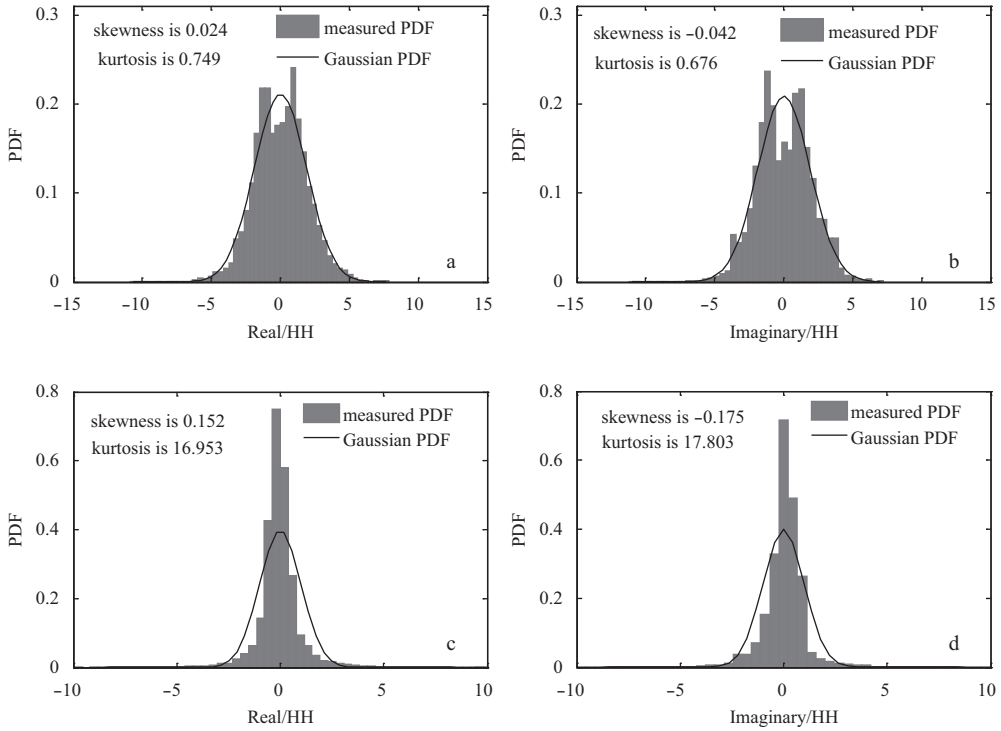

Fig. 4. The histograms of the real (left) and imaginary (right) parts of the sea clutter data. The above and below patterns correspond to the real sea clutter S^{s}_{HH} and the raw data S_{HH}, respectively.

ments of scattering matrix are both satisfying circular Gaussian distribution (Goodman, 1985), based on the complex Wishart distribution model, the distribution of the n-look covariance matrix $Z(\tau)$ is derived as

$$P_z(\boldsymbol{Z})=\frac{n^{n-m+1}|\boldsymbol{Z}|^{n-m}\exp\left[-n\mathrm{tr}(\boldsymbol{C}^{-1}\boldsymbol{Z})\right]}{K(n,m)|\boldsymbol{C}|^{n}}, \tag{15}$$

where $\mathrm{tr}(\bullet)$ denotes the trace of $\boldsymbol{C}^{-1}\boldsymbol{Z}$; $K(n,m)=\pi^{\frac{1}{2}m(m-1)}\Gamma(n)\cdots\Gamma(n-m+1)$, m is the dimension of vector $\vec{u}$, and $\Gamma(\bullet)$ denotes the Gamma function; and $\boldsymbol{C}$ is the complex covariance matrix and it can be written as

$$\boldsymbol{C}=\langle\vec{u}(t)\vec{u}(t')^{*\mathrm{T}}\rangle=\begin{bmatrix}\langle|S_{pq}(t')|^2\rangle & \langle S_{pq}(t')S^{*}_{uv}(t)\rangle\\ \langle S^{*}_{pq}(t')S_{uv}(t)\rangle & \langle|S_{uv}(t)|^2\rangle\end{bmatrix}. \tag{16}$$

For the case of $m=1$ and $\tau=0$, using Eq. (15), the one-dimensional n-look intensity distribution can be simplified as

$$P_{Z_{11}}(Z_{11})=\frac{n^{n}|Z_{11}|^{n-1}\exp\left[-n(Z_{11}/C_{11})\right]}{\Gamma(n)C_{11}^{n}}. \tag{17}$$

For the case of $m=2$, if we set $\boldsymbol{A}=n\boldsymbol{Z}$ and $t'=t+\tau$, using Eqs (13) and (14), it is obtained that

$$\boldsymbol{C}=\begin{bmatrix}C_{11} & \sqrt{C_{11}C_{22}}|\rho|e^{j\bar{\phi}}\\ \sqrt{C_{11}C_{22}}|\rho|e^{-j\bar{\phi}} & C_{22}\end{bmatrix}, \tag{18}$$

$$\boldsymbol{A}=\begin{bmatrix}A_{11} & \alpha e^{j\phi}\\ \alpha e^{-j\phi} & A_{22}\end{bmatrix}, \tag{19}$$

where $C_{11}=\langle S_{pq}(t+\tau)S^{*}_{pq}(t+\tau)\rangle$; $C_{22}=\langle S_{uv}(t)S^{*}_{uv}(t)\rangle$; $\alpha e^{j\phi}=A_{12}=A_{12R}+jA_{12I}$, and $\phi=\mathrm{Arg}\left[\sum_{k=1}^{n}S_{pq}(t_k+\tau)S^{*}_{uv}(t_k)\right]$ denotes the phase difference; the normalized cross-complex correlation coefficient ρ is

$$\rho(\tau)=|\rho|e^{j\phi}=\frac{\langle S_{pq}(t+\tau)S^{*}_{uv}(t)\rangle}{\sqrt{\langle|S_{pq}(t+\tau)|^2\rangle\langle|S_{uv}(t)|^2\rangle}}. \tag{20}$$

Substituting Eqs (18) and (19) into Eq. (15), the joint probability density function of A_{11}, A_{22}, A_{12R} and A_{12I} is obtained that

$$\begin{aligned}P(A_{11},A_{22},A_{12R},A_{12I})=&\\ &\frac{\left(A_{11}A_{22}-A_{12R}^2-A_{12I}^2\right)^{n-2}}{n\Gamma(n)\Gamma(n-1)\left\{C_{11}C_{22}\left(1-|\rho|^2\right)\right\}^{n}}\times\\ &\exp\left[-\frac{A_{11}C_{22}+A_{22}C_{11}}{C_{11}C_{22}\left(1-|\rho|^2\right)}\right]\times\\ &\exp\left[\frac{2|\rho|\sqrt{C_{11}C_{22}}\left(\cos\bar{\phi}A_{12R}+\sin\bar{\phi}A_{12I}\right)}{C_{11}C_{22}\left(1-|\rho|^2\right)}\right].\end{aligned} \tag{21}$$

Because the covariance matrix $\boldsymbol{A}$ is positive-definite, the integration domain is constrained by $(A_{11}A_{22}-A_{12R}^2-A_{12I}^2)>0$. Thus, The PDF $P(A_{12R},A_{12I})$ can be obtained by

$$P(A_{12R},A_{12I})=\int_0^{+\infty}\int_{(A_{12R}^2+A_{12I}^2)/A_{22}}^{+\infty}\frac{\left(A_{11}A_{22}-A_{12R}^2-A_{12I}^2\right)^{n-2}}{n\Gamma(n)\Gamma(n-1)\left\{C_{11}C_{22}\left(1-|\rho|^2\right)\right\}^n}\times \exp\left[-\frac{A_{11}C_{22}+A_{22}C_{11}}{C_{11}C_{22}\left(1-|\rho|^2\right)}\right]\times \exp\left[\frac{2|\rho|\sqrt{C_{11}C_{22}}\left(\cos\bar{\phi}A_{12R}+\sin\bar{\phi}A_{12I}\right)}{C_{11}C_{22}\left(1-|\rho|^2\right)}\right]\mathrm{d}A_{11}\mathrm{d}A_{22}. \quad (22)$$

Then integrating Eq. (22) respect to A_{11} and A_{22}, after a tedious but direct mathematical derivation, we can obtain that

$$P(A_{12R},A_{12I})=\frac{2n^{\frac{n-1}{2}}\left(A_{12R}^2+A_{12I}^2\right)^{\frac{n-1}{2}}}{\pi\Gamma(n)(C_{11}C_{22})^{\frac{n+1}{2}}\left(1-|\rho|^2\right)}\times \exp\left[\frac{2|\rho|\left(\cos\bar{\phi}A_{12R}+\sin\bar{\phi}A_{12I}\right)}{\sqrt{C_{11}C_{22}}\left(1-|\rho|^2\right)}\right]\times \mathrm{K}_{n-1}\left[\frac{2\sqrt{A_{12R}^2+A_{12I}^2}}{\sqrt{C_{11}C_{22}}\left(1-|\rho|^2\right)}\right], \quad (23)$$

where K_{n-1} is the second kind modified Bessel function of $n-1$ order. Because $\boldsymbol{A}=n\boldsymbol{Z}$, the joint PDF of Z_{12R} and Z_{12I} can be obtained directly by the identity $P(Z_{12R},Z_{12I})\mathrm{d}Z_{12R}\mathrm{d}Z_{12I}=P(A_{12R},A_{12I})\mathrm{d}A_{12R}\mathrm{d}A_{12I}$ as

$$P(Z_{12R},Z_{12I})=\frac{2n^{n+1}\left(Z_{12R}^2+Z_{12I}^2\right)^{\frac{n-1}{2}}}{\pi\Gamma(n)(C_{11}C_{22})^{\frac{n+1}{2}}\left(1-|\rho|^2\right)}\times \exp\left[\frac{2n|\rho|\left(\cos\bar{\phi}Z_{12R}+\sin\bar{\phi}Z_{12I}\right)}{\sqrt{C_{11}C_{22}}\left(1-|\rho|^2\right)}\right]\times \mathrm{K}_{n-1}\left[\frac{2n\sqrt{Z_{12R}^2+Z_{12I}^2}}{\sqrt{C_{11}C_{22}}\left(1-|\rho|^2\right)}\right]. \quad (24)$$

Then integrating Eq. (24) with respect to Z_{12R} yields

$$P(Z_{12I})=\frac{2n^{n+1}}{\pi\Gamma(n)(C_{11}C_{22})^{\frac{n+1}{2}}\left(1-|\rho|^2\right)}\times \exp\left(\frac{2n|\rho|\sin\bar{\phi}Z_{12I}}{\sqrt{C_{11}C_{22}}\left(1-|\rho|^2\right)}\right)\times \left\{\sum_{k=0}^{\infty}\frac{\left(a|\rho|\cos\bar{\phi}\right)^k}{k!}\int_0^{\infty}Z_{12R}^k\left(\sqrt{Z_{12R}^2+Z_{12I}^2}\right)^{n-1}\times \mathrm{K}_{n-1}\left(a\sqrt{Z_{12R}^2+Z_{12I}^2}\right)\mathrm{d}Z_{12R}+\sum_{k=0}^{\infty}\frac{\left(a|\rho|\cos\bar{\phi}\right)^k}{k!}\times \int_0^{\infty}Z_{12R}^k\left(\sqrt{Z_{12R}^2+Z_{12I}^2}\right)^{n-1}\times \mathrm{K}_{n-1}\left(a\sqrt{Z_{12R}^2+Z_{12I}^2}\right)\mathrm{d}Z_{12R}\right\}. \quad (25)$$

Applying an integration identity from Gradshteyn and Ryzhik (2007), Eq. (25) can be simplified as

$$P(Z_{12I})=\frac{2an^n}{\pi\Gamma(n)(C_{11}C_{22})^{\frac{n}{2}}}\exp\left(a|\rho|\sin\bar{\phi}Z_{12I}\right)\times \sum_{k=0}^{\infty}\frac{\left(a|\rho|\cos\bar{\phi}\right)^{2k}}{(2k)!}\frac{2^{(2k-1)/2}\Gamma\left(\frac{2k+1}{2}\right)}{a^{(2k+1)/2}}\times |Z_{12I}|^{n+\frac{2k-1}{2}}\mathrm{K}_{n+\frac{2k-1}{2}}\left(a|Z_{12I}|\right), \quad (26)$$

and the parameter $a=\frac{2n}{\sqrt{C_{11}C_{22}}\left(1-\rho^2\right)}$.

In the same way, integrating Eq. (24) over Z_{12I}, the PDF of the parameter Z_{12R} is derived as

$$P(Z_{12R})=\frac{2an^n}{\pi\Gamma(n)(C_{11}C_{22})^{\frac{n}{2}}}\exp\left(a|\rho|\cos\bar{\phi}Z_{12R}\right)\times \sum_{k=0}^{\infty}\frac{\left(a|\rho|\sin\bar{\phi}\right)^{2k}}{(2k)}\frac{2^{(2k-1)/2}\Gamma\left(\frac{2k+1}{2}\right)}{a^{(2k+1)/2}}|Z_{12R}|^{n+\frac{(2k-1)}{2}}\mathrm{K}_{n+\frac{(2k-1)}{2}}\left(a|Z_{12R}|\right). \quad (27)$$

Using the identities $P(|Z_{12}|,\phi)\mathrm{d}|Z_{12}|\mathrm{d}\phi=P(Z_{12R},Z_{12I})\mathrm{d}Z_{12R}\mathrm{d}Z_{12I}$ and $\mathrm{d}Z_{12R}\mathrm{d}Z_{12I}=|Z_{12}|\mathrm{d}|Z_{12}|\mathrm{d}\phi$, the polar form of Eq. (24) is obtained as

$$P(|Z_{12}|,\phi)=\frac{2n^{n+1}|Z_{12}|^n}{\pi\Gamma(n)(C_{11}C_{22})^{\frac{n-1}{2}}\left(1-|\rho|^2\right)}\times \exp\left[\frac{2n|\rho||Z_{12}|\cos\left(\phi-\bar{\phi}\right)}{\sqrt{C_{11}C_{22}}\left(1-|\rho|^2\right)}\right]\times \mathrm{K}_{n-1}\left[\frac{2n|Z_{12}|}{\sqrt{C_{11}C_{22}}\left(1-|\rho|^2\right)}\right]. \quad (28)$$

Then integrating Eq. (28) over $|Z_{12}|$ (or ϕ), the PDF of the phase difference ϕ (or the intensity $|Z_{12}|$) is obtained as

$$P(\phi)=\frac{\Gamma(n+0.5)\left(1-|\rho^2|\right)^n\beta}{2\sqrt{\pi}\Gamma(n)\left(1-\beta^2\right)^{n+0.5}}+\frac{\left(1-|\rho^2|\right)^n}{2\pi}F\left(n,1;1/2;\beta^2\right), \quad (29)$$

and

$$P(|Z_{12}|)=\frac{4n^{n+1}|Z_{12}|^n}{\Gamma(n)(C_{11}C_{22})^{\frac{n+1}{2}}\left(1-|\rho|^2\right)}\times \mathrm{I}_0\left[\frac{2n|\rho||Z_{12}|}{\sqrt{C_{11}C_{22}}\left(1-|\rho|^2\right)}\right]\times \mathrm{K}_{n-1}\left[\frac{2n|Z_{12}|}{\sqrt{C_{11}C_{22}}\left(1-|\rho|^2\right)}\right], \quad (30)$$

where $\beta=|\rho|\cos\left(\phi-\bar{\phi}\right)$; and $F\left(n,1;1/2;\beta^2\right)$ is a Gauss hypergeometric function. For $n=1$, $F\left(1,1;1/2;\beta^2\right)=\left(1-\beta^2\right)^{-1}\left[1+\frac{\beta\arcsin\beta}{\sqrt{1-\beta^2}}\right]$. I_0 represents the 0-order modified Bessel function of the first kind.

4 Comparisons of theoretical PDFs with measurements

In Fig. 5, the statistics of the phase differences are estimated from the actual sea clutter data obtained by different radar channels. In the left graphs, the theoretical results (dash lines) evaluated by Eq. (29) are compared with the measurements (solid lines). From Fig. 5, we can find that the theoretical contour lines have the same shapes with the measurements in spite of the small deviation. For the same time lag, the measured phase difference is slightly lower than the theoretical results evaluated by Eq. (29). This deviation between the theoretical result and the measurement is mainly caused by the inhomogeneity of the actual sea clutter. Because the correlation defined by Eq. (20) averages over all the valid sea clutter, the correlation coefficient $|\rho|$ and the mean phase difference $\bar{\phi}$ would be dominated by the signals whose intensity is higher. Therefore, in order to eliminate the impact of the inhomogeneity of the sea clutter, instead of Eq. (20), the correlation function average over a short-time interval is used to estimate $|\rho|$ and $\bar{\phi}$ (Chapman et al., 1994). The short-time correlation function is defined as

$$\rho'(\tau)=\frac{\left\langle S^{s}_{pq}(t+\tau)S^{s^*}_{uv}(t)\right\rangle|_{T}}{\sqrt{\left\langle\left|S^{s}_{pq}(t+\tau)\right|^2\right\rangle\left\langle\left|S^{s}_{uv}(t)\right|^2\right\rangle}|_{T}}, \tag{31}$$

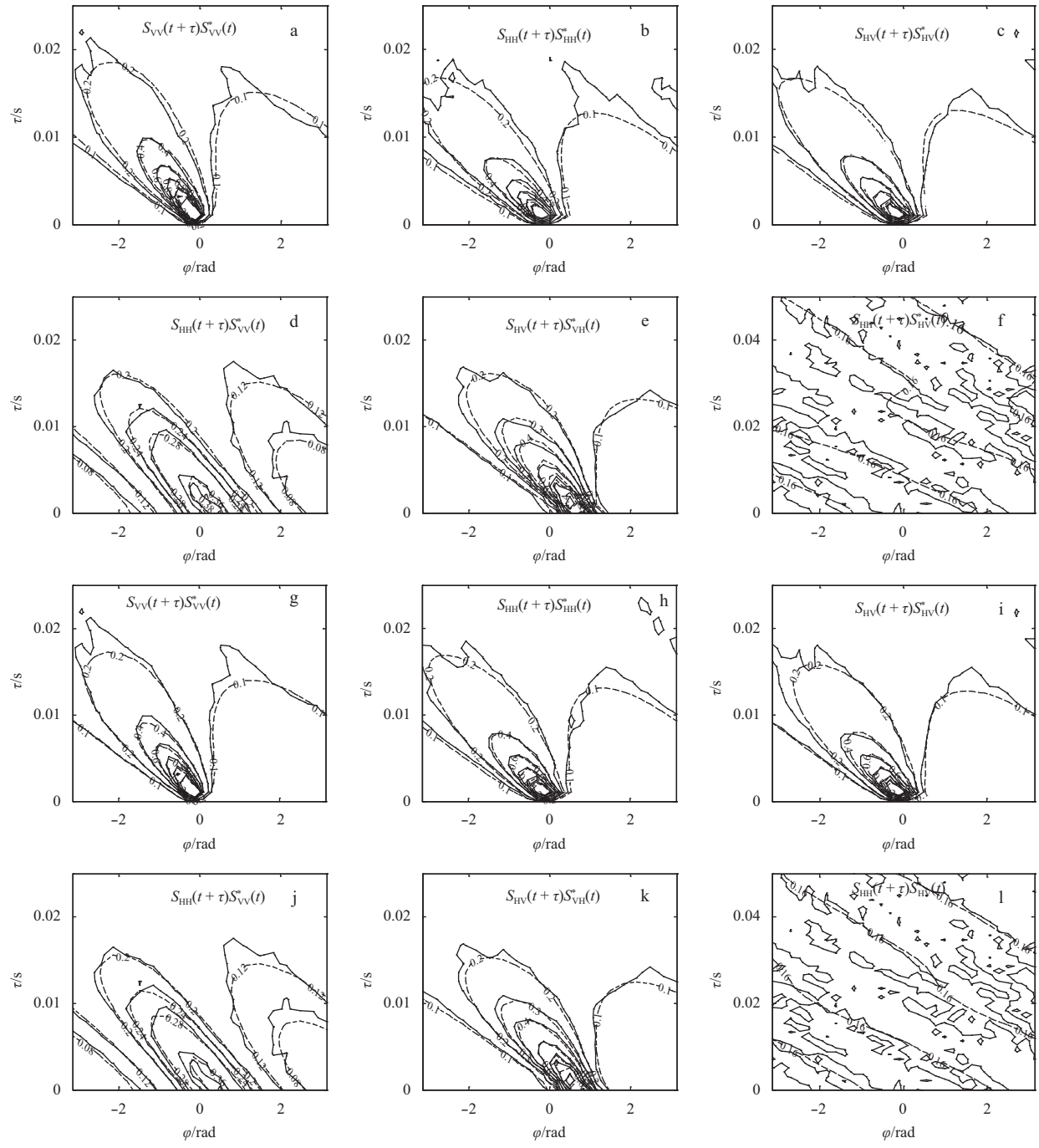

Fig. 5. The contour lines of the theoretical (dash) and measured (solid) phase difference distributions. In the theoretical models, $|\rho|$ and $\bar{\phi}$ are evaluated by Eq. (20) (Figs 5a–f) and Eq. (31) (Figs 5g–l), respectively.

where $\langle\bullet\rangle_T$ denotes average overtime interval T. In the present work, the time interval T is set to 0.1 s. Substituting $|\rho|$ and $\bar{\phi}$ evaluated by Eq. (31) into Eq. (29), the theoretical model of the phase difference should become more reasonable. From the right graphs of Fig. 5, we can find that the theoretical model is somewhat improved. For the time series (such as $S^s_{HH}(t+\tau)S^{s*}_{HH}(t)$, $S^s_{VV}(t+\tau)S^{s*}_{VV}(t)$, $S^s_{VH}(t+\tau)S^{s*}_{VH}(t)$, $S^s_{HV}(t+\tau)S^{s*}_{HV}(t)$) obtained by a radar channel, just as expected, there are no phase differences at time lag τ=0. However, with the increase of the time lag, the absolute values of the mean phase differences (i.e., the phase differences at the peaks of the PDFs) are linearly increased. Here, the mean phase differences are negative because the waves propagated far away from the radar. Of course, if the waves propagated toward the radar, the mean phase differences would be positive. Form the figures it is also found that the PDFs are also broadened with the time lag, and in the limit of long lag time the scattered field would de-correlate and the phase differences would be uniformly distributed between – π and π. From Fig. 5, we can find that the limit decorrelation time lag is about 20 ms for X-band radar.

It is well known that for the backscattered fields the reciprocity theorem is satisfied, i.e., $S^s_{HV}(t)=S^s_{VH}(t)$. Thus, at the time lag τ=0 s, the equation $\arg\left[S^s_{HV}(t)S^{s*}_{VH}(t)\right]=0$ should be true. However, the PDFs in Figs 5i and j show that at a time lag of 0 ms the mean phase difference between $S^s_{HV}(t)$ and $S^s_{VH}(t)$ is not equal to 0 and the value of it is about 0.65 rad. The deviation with the reciprocity theorem is probably caused by the original phase difference between the horizontal and vertical polarized pulses. Of course, from the mean phase difference between $S^s_{HH}(t)$ and $S^s_{VV}(t)$ in Figs 5g and h, the original phase difference between the horizontal and vertical polarized pulses can also be found. On the basis of the Bragg theory, there will no phase differences between S^s_{HH} and S^s_{VV} at the time lag τ=0 s. However, just as the results shown in Figs 5i and j, at a time lag of 0 ms the mean phase difference between S^s_{HH} and S^s_{VV} is also about 0.65 rad. In this work, the distributions of the phase differences between the co- and cross-polarization channels are also discussed. However, for the sake of saving space, only the distributions of the phase differences between S^s_{HH} and S^s_{HV} are presented in Figs 5k to l. Just as we expected, the co- and cross-polarization channels are uncorrelated with each other, and then the phase differences between co- and cross- polarization channels are almost uniformly distributed in the interval from – π to π.

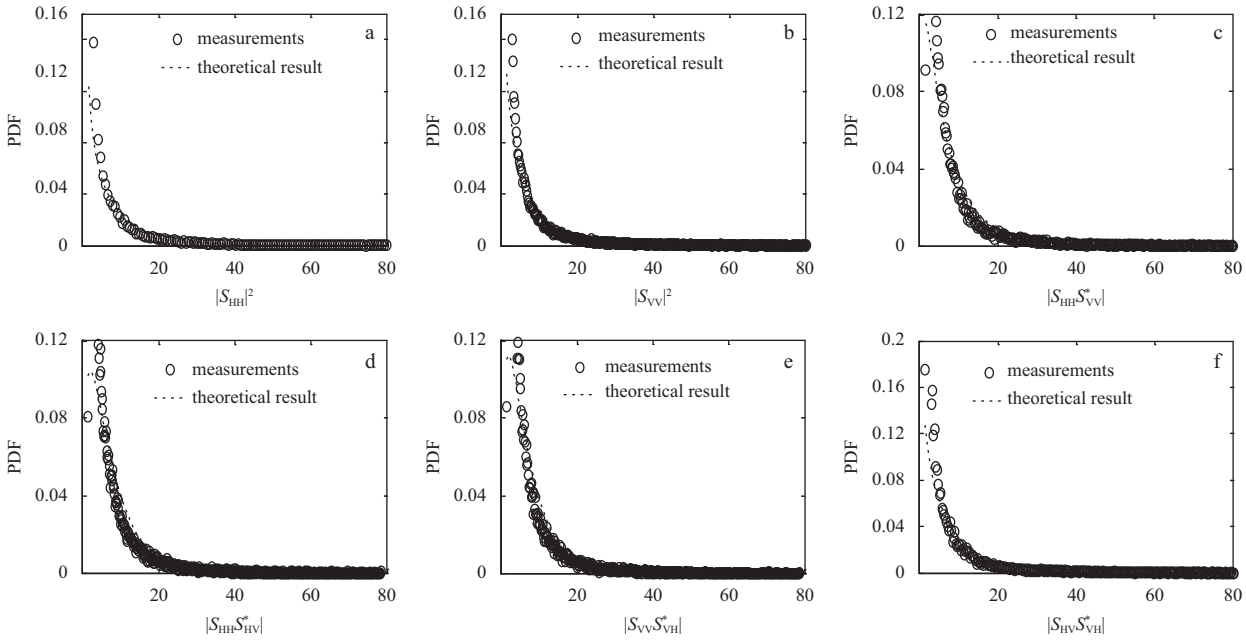

Fig. 6. The PDFs of the intensities in the complex covariance matrix.

The distributions of the intensities of the elements in the complex covariance matrix are shown in Fig. 6. The theoretic PDFs are simulated by Eq. (30). As shown in the figures, the theoretical PDFs fit the measured data well. On the other hand, we can also find that the curves in Fig. 6 just like the negative exponential distributions. This conclusion is consistent with the theoretic result obtained in Lee et al. (1994a, b).

The theoretical PDFs of the real and imaginary parts of the elements in the complex covariance matrix are illustrated in Fig. 7. Here, the value of the time lag τ is set to 0. In Figs 7a–h, from the distributions between the co- and the cross– polarizations channels it is found that whether the distributions of real parts or the distributions of imaginary parts are all symmetric around 0. This symmetry is due to the fact that the phase differences between co- and cross-polarization channels are almost uniformly distributed in the interval from – π to π. However, the distributions in Figs 7i–l are not symmetric around 0. The curves in Figs 7i–l show that the real and the imaginary parts of $S^s_{HH}(t)S^{s*}_{VV}(t)$ and $S^s_{HV}(t)S^{s*}_{VH}(t)$ are mostly greater than 0. This paradoxical phenomenon is mainly induced by the original phase difference between the horizontal and vertical polarized channels of the IPIX radar. Just as shown in Fig. 5, this original phase difference is about 0.65 rad. Here, we should point out that, in view of the limited space, the comparisons between the theoretical results and the measurements for the case of $\tau\neq 0$ are not shown in this paper.

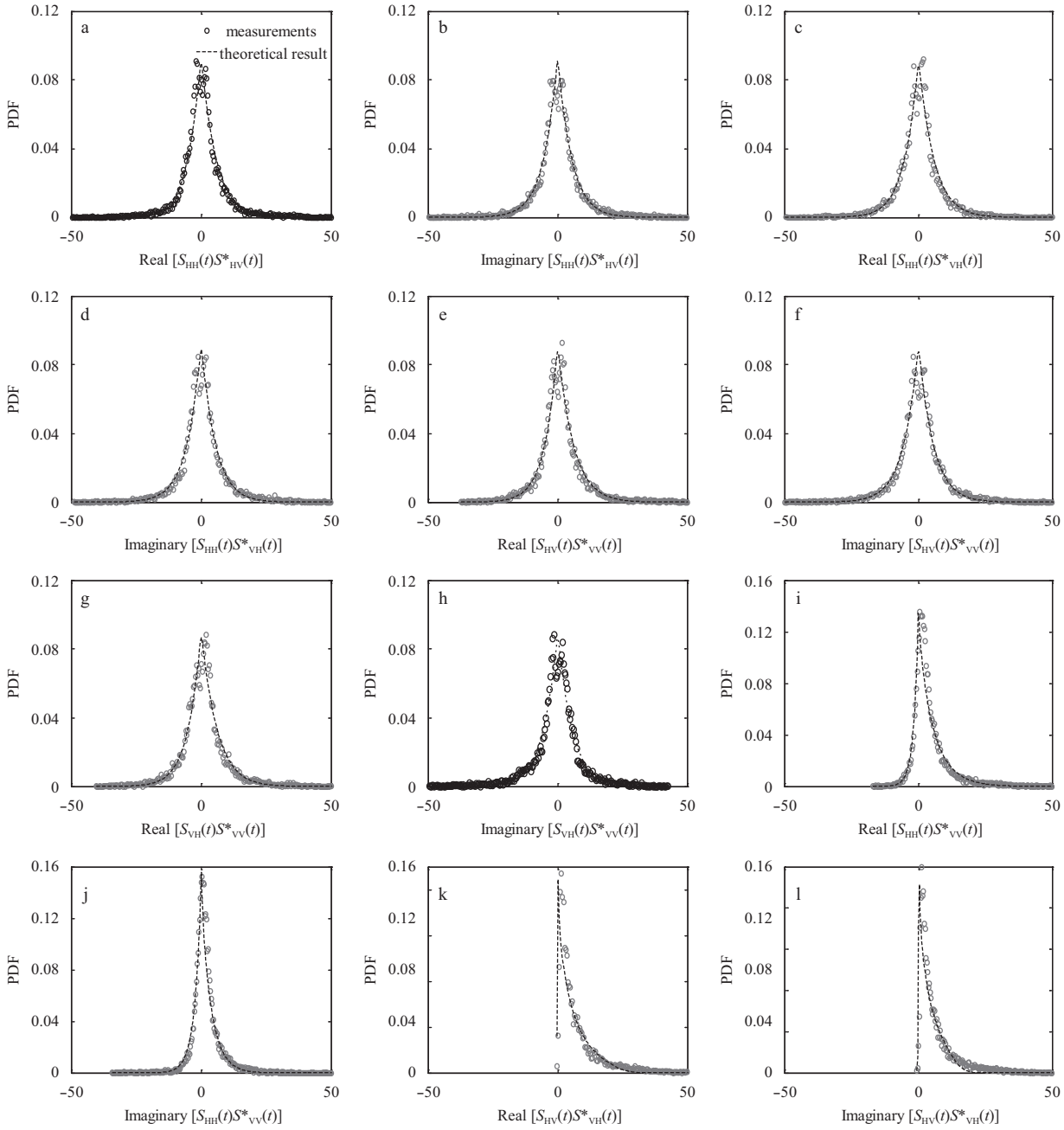

Fig. 7. The theoretical PDFs of the real and imaginary parts of the elements in the complex covariance matrix. The dashed line and the circles correspond to the theoretical and measurement results, respectively.

5 Conclusions

The statistical characterizations of the pol-radar signals backscattered from the sea surface have been investigated. The probability density distribution functions of the intensity, the phase difference, the real and imaginary parts of the elements in the covariance matrix have been derived theoretically. The results presented in this work demonstrate that the shadow of the large-scale waves will cause remarkable influence on the statistic properties of the echoes backscattered from the sea surface at low grazing angles. In the shadow regions of large-scale waves, the echoes are mainly dominated by the noise of the radar system. Just as expected, the theoretical models can fit the measurements well if we remove the echoes from the shadow regions. On the other hand, the results also show that the inhomogeneity of the real sea clutter will also cause somewhat effect on the statistic properties. The accuracy of the theoretical models can be improved slightly if we evaluate the correlation coefficient and the mean phase difference by the short-time normalized correlation function.

In this work, the real sea clutter and the noise of the radar system are simply separated by a plausible threshold value. However, how to strictly judge where are the shadow regions should be further investigated.

Acknowledgements

The IPIX radar data were provided by the Cognitive Systems Laboratory, McMaster University.

References

Brusch S, Lehner S, Fritz T, et al. 2011. Ship surveillance with TerraSAR-X. IEEE Transactions on Geoscience and Remote Sensing, 49(3): 1092–1103

Chapman R D, Gotwols B L, Sterner R E. 1994. On the statistics of the phase of microwave backscatter from the ocean surface. Journal of Geophysical Research, 99(C8): 16293–16301

Conte E, De Maio A, Galdi C. 2004. Statistical analysis of real clutter at different range resolutions. IEEE Transactions on Aerospace and Electronic Systems, 40(3): 903–918

Conte E, Longo M, Lops M. 1991. Modelling and simulation of non-Rayleigh radar clutter. IEE Proceedings F-Radar and Signal Processing, 138(2): 121–130

Cui Limin, He Yijun, Shen Hui, et al. 2010. Measurements of ocean wave and current field using dual polarized X-band radar. Chinese Journal of Oceanology and Limnology, 28(5): 1021–1028

Farina A, Gini F, Greco M V, et al. 1997. High resolution sea clutter data: statistical analysis of recorded live data. IEE Proceedings-Radar, Sonar and Navigation, 144(3): 121–130

Farina A, Russo A, Studer F A. 1986. Coherent radar detection in log-normal clutter. IEE Proceedings F-Communications, Radar and Signal Processing, 133(1): 39–53

Goodman N R. 1963. Statistical analysis based on a certain multivariate complex Gaussian distribution (an introduction). The Annals of Mathematical Statistics, 34(1): 152–177

Goodman J W. 1985. Statistical Optics. New York: John Wiley & Sons

Gradshteyn I S, Ryzhik I M. 2007. Table of Integrals, Series, and Products. 7th ed. London: Academic

Greco M, Bordoni F, Gini F. 2004. X-band sea-clutter nonstationarity: influence of long waves. IEEE Journal of Oceanic Engineering, 29(2): 269–283

Hwang P A, Sletten M A, Toporkov J V. 2008. Breaking wave contribution to low grazing angle radar backscatter from the ocean surface. Journal of Geophysical Research, 113(C9): C09017

Johnson J T, Burkholder R J, Toporkov J V, et al. 2009. A numerical study of the retrieval of sea surface height profiles from low grazing angle radar data. IEEE Transactions on Geoscience and Remote Sensing, 47(6): 1641–1650

Kuttikkad S, Chellappa R. 1994. Non-Gaussian CFAR techniques for target detection in high resolution SAR images. In: IEEE International Conference in Image Processing. Vol. 1. Austin, TX: IEEE, 910–914

Lee P H Y, Barter J D, Beach K L, et al. 1995. X-band microwave backscattering from ocean waves. Journal of Geophysical Research, 100(C2): 2591–2611

Lee J S, Hoppel K W, Mango S A, et al. 1994a. Intensity and phase statistics of multilook polarimetric and interferometric SAR imagery. IEEE Transactions on Geoscience and Remote Sensing, 32(5): 1017–1028

Lee J S, Miller A R, Hoppel K W. 1994b. Statistics of phase difference and product magnitude of multi-look processed Gaussian signals. Waves in Random Media, 4(3): 307–319

Posner F L. 2002. Spiky sea clutter at high range resolutions and very low grazing angles. IEEE Transactions on Aerospace and Electronic Systems, 38(1): 58–73

Vachon P W, Campbell J W M, Bjerkelund C A, et al. 1997. Ship detection by the RADARSAT SAR: validation of detection model predictions. Canadian Journal of Remote Sensing, 23(1): 48–59

Wang Yunhua, Li Huimin, Zhang Yanmin, et al. 2015. The measurement of sea surface profile with X-band coherent marine radar. Acta Oceanologica Sinica, 34(9): 65–70

Yang Y, Xiao S P, Wang X S, et al. 2017. Statistical distribution of polarization ratio for radar sea clutter. Radio Science, 52(8): 981–987, doi: 10.1002/2017RS006371

Zhu Hong, Wang Qingping, Tai Ning, et al. 2017. Statistical analysis of high-resolution coherent monopulse radar sea clutter. International Journal of Antennas and Propagation, 2017: 7471918